POLITECNICO DI TORINO
Repository ISTITUZIONALE

Sustainable, economic, and simple preparation of an efficient catalyst for Li–O2 batteries

Original
Sustainable, economic, and simple preparation of an efficient catalyst for Li–O2 batteries / Amici, J., Marquez, P., Mangini, A., Torchio, C., Dessantis, D., Versaci, D., Francia, C., Aguirre, M.J., Bodoardo, S.. - In: JOURNAL OF POWER SOURCES. - ISSN 0378-7753. - ELETTRONICO. - 546:(2022), p. 231942. [10.1016/j.jpowsour.2022.231942]

Availability:
This version is available at: 11583/2971397 since: 2022-09-18T15:37:28Z

Publisher:
Elsevier B.V.

Published
DOI:10.1016/j.jpowsour.2022.231942

Terms of use:

This article is made available under terms and conditions as specified in the corresponding bibliographic description in the repository

Publisher copyright
Elsevier postprint/Author's Accepted Manuscript

© 2022. This manuscript version is made available under the CC-BY-NC-ND 4.0 license
http://creativecommons.org/licenses/by-nc-nd/4.0/.The final authenticated version is available online at:
http://dx.doi.org/10.1016/j.jpowsour.2022.231942

(Article begins on next page)

10 September 2026

Sustainable, economic, and simple preparation of an efficient catalyst for Li-O_2 batteries

Julia Amici [a], Paulina Marquez [b], Anna Mangini [a], Claudia Torchio [a], Davide Dessantis [a], Daniele Versaci [a], Carlotta Francia [a], María Jesus Aguirre [c], Silvia Bodoardo [a]*

[a] Department of Applied Science and Technology (DISAT), Politecnico di Torino, C.so Duca degli Abruzzi 24, 10129 Torino, Italy

[b] Escuela de Ingeniería, Universidad Central de Chile, 8330601 Santiago, Chile

[c] Departamento de Química de los Materiales, Facultad de Química y Biología, Universidad de Santiago de Chile (USACH), Av. B. O'Higgins 3363, Estación Central, Santiago, Chile.

*Corresponding author: julia.amici@polito.it

Abstract

Developing efficient electrocatalysts for oxygen reduction reaction (ORR) is fundamental to bring the Li-O_2 technology closer to practical applications. However, the majority of studied catalysts for this application are either precious metals or cobalt based, which represents an obstacle for a larger scale development, both from an economical and a political point of view. In this work a simple, fully sustainable, and economic synthesis process is used to *in situ* nucleate SnO_2 nanoparticles on the surface of commercial carbon black (C45) by taking advantage of its numerous nucleation sites to deposit and chemically anchor SnO_2 nanoparticles. Such synthesis can easily be carried out through wet impregnation, without any acid treatment or high temperature process. The obtained composite material shows an optimal ORR activity, which is confirmed in Li-O_2 cells. Indeed, compared to pure C45 air-cathodes, the composite cathodes lead to the formation of much more reversible film-like discharge products, allowing for reduced overvoltage and therefore improved cycling performances both at the high current density of 0.5 mA cm^{-2} with more than 70 cycles and in prolonged discharge/charge conditions with over 1250 h of operation at the fixed capacity of 2.5 mAh cm^{-2}.

Keywords: Li-O_2 battery, ORR catalyst, air cathode, sustainability, energy storage

1. Introduction

With the shortage of non-renewable fossil fuels and an ever-growing awareness of global warming associated issues, efficient energy storage technologies seem to be a more reliable solution [1]. The Li-ion technology, widely studied and available on the market for multiple application is now reaching its limits and while a lot of studies are still carried out, for example on new cathode materials [2] or directly using metallic lithium anode [3], it does not represent alone a viable option toward energetic transition [4]. The lithium−oxygen (Li-O_2) battery, based on the electrochemical reaction $2Li^+ + O_2 + 2e^- \rightleftharpoons Li_2O_2$ (E_0 = 2.96 V vs Li^+/Li) is recognized as one of the promising candidates for energy storage, primarily due to its superhigh theoretical energy density of 3505 Wh kg^{-1}, which is 10 times higher than the one of Li-ion batteries and comparable to the one of gasoline, as well as to its ability to obtain the cathode active material, oxygen, directly from air instead of being provided internally [5–8]. However, many challenges remain to be solved before this technology can actually represent an industrial reality, indeed the cell is affected by high overpotentials, poor rate capability and low cycling performances. The reasons for these drawbacks are manifolds, but one of the most important lays on the nature of the typical discharge product Li_2O_2, which possesses sluggish charge transfer kinetics, necessitating therefore high potential for its decomposition, resulting in inferior rate capability and poor energy efficiency [9]. In addition, such high potentials, are inevitably linked to parasitic reactions, such as electrolyte or carbon cathode decompositions, generating more insulating side products.

For this reason, cathode design is the keystone towards Li-O_2 batteries upscaling. In this view, a lot of studies have been carried out on oxygen reduction reaction (ORR) and oxygen evolution reaction (OER) catalysts. Noble metals and their oxides, such as Pt [10], Ru [11], Pd [12], RuO_2 [13,14] have largely proved their efficiency as bifunctional catalysts, however their cost and

scarcity do not qualify them as proper solutions for the industrial scale. Among the non-precious metal family, Co and its oxides have been the elements of major success in the field, for both ORR and OER [14–19], nonetheless Co is now officially classified as a critical raw material, both for its scarcity and for its way of extraction, and therefore its use should be avoided as much as possible. Another transition metal of interest for this application is Mo, recent works have shown really interesting results of Mo-based bifunctional catalysts [1,20–22], although they all report quite complicated and costly preparation process both from an economical and from an energetical point of view.

Among metal oxides, tin dioxide (SnO_2) has several applications in gas sensing thanks to its strong interplay with O_2 [8,23], as well as in lithium-ion batteries, exhibiting a high lithium storage capacity and an excellent cycling performance [7,24,25], moreover SnO_2 is a low-cost raw material [26], that recently has been considered as a promoter catalyst for both ORR and OER in the Li-O_2 air-cathode [7,8,27,28]. However, to obtain SnO_2 nanoparticles on a conductive matrix, all the methods reported [7,8,27,28] involve either magnetron sputtering or high temperature calcination therefore, these complex and expensive syntheses limit the benefits of using such inexpensive precursors.

In this work a simple, fully sustainable, and economic synthesis process previously studied for the preparation of Li-ion anodic material [25], is used to *in situ* nucleate SnO_2 nanoparticles on the surface of commercial carbon black C-NERGY TM Super C45 (Imerys Graphite & Carbon). Such synthesis was carried out by wet impregnation without any acid treatment or high temperature process. After a precise assessment of the catalytic activity of the obtained composite material, demonstrating its advantages for the ORR process, it was used to prepare air cathodes over a commercial gas diffusion layer. To date, most published studies on ORR catalysts for Li-O_2 applications are difficult to compare, because of different test parameters such as applied current density, fixed capacity and catalyst areal loading. Therefore, in this work, we report the obtained results as areal capacities to facilitate the comparison with recent

State of Art, observing improved cycling performances both at the high current density of 0.5 mA cm^{-2} with more than 70 cycles and in prolonged discharge/charge process with over 1250 h of operation at the fixed capacity of 2.5 mAh cm^{-2} (see Table S1).

2. Experimental Section

2.1 Materials preparation

As previously reported [25], the synthesis of SnO_2@C45 consists in two simple steps: in situ deposition of SnO_2 on C45 followed by elimination of the impurities. In situ deposition of SnO_2 was achieved by pouring an aqueous solution of $SnCl_2 \bullet 2H_2O$ (purity > 98%, Sigma-Aldrich) on commercial carbon black (TIMCAL C-NERGY TM Super C45- Imerys) to obtain a semi-solid sludge with Sn/C = 2/3 (mass ratio). Typically, 1.2g of $SnCl_2 \bullet 2H_2O$ were dissolved into 12 g of Milli-Q ® water to obtain a 9.0% w/w milky suspension (pH = 1.74). Then 2.0 g of C45 were added to the suspension under stirring at room temperature. Finally, the sludge was dried overnight at 80 °C, to obtain the raw SnO_2@C45 material. In the second step, the removal of impurities was carried out by washing the sample with water and centrifuging (10,000 rpm for 15 min) several times until reaching a pH value around 4.0. The so obtained product was dried overnight at 80°C and is successively referred to as SnO_2@C45.

2.2 Material characterization

The thermal stability and the amount of SnO_2 were detected by TGA in air from room temperature to 800 °C, at the heating rate of 10 °C min^{-1} using a LINSEIS STA PT1600.

XRD analysis was carried out by a PANalytical X'Pert (Cu Ka radiation) diffractometer. Data were collected with a 2D solid state detector (PIXcel) from 10 to 80 ° with a step size of 0.026 ° s^{-1}.

FESEM analysis was carried out by Zeiss SUPRA TM 40 with Gemini column and Schottky field emission tip (tungsten at 1800 K). Acquisitions were made at acceleration voltage of 3 kV and working distance (WD) between 2.1 and 8.5 mm, with magnification up to 1000 Kx.

The scanning/transmission electron microscope (S/TEM) analysis was carried out using a Thermo Scientific TM Talos F200X.

2.3 Electrochemical measurements

In order to assess the catalytic activity of the material, an ink was prepared with 5 mg of active material (C45 or SnO_2@C45), 833 µL of deionized water, 167 µL isopropanol and 20 µL of 5% Nafion solution, followed by 30 min of ultrasonic treatment [1]. Then, 3 µL of ink were deposited on a glassy carbon surface and oven-dried at 90°C to form a smooth film. The final catalyst loading was 0.1 mg cm^{-2}.

Electrochemical measurements were carried out using a bipotentiostat (CHI900B) in a three-compartment electrochemical cell. A rotating ring disk electrode, (RRDE) (AFE6RIPT model, Pine) with a disk of glassy carbon, (5 mm diameter) and a ring of Pt were used as working electrodes. A Pt wire was the counter electrode and Ag/AgCl (KCl sat.) was the reference electrode connected to the compartment of the working electrodes by a Luggin capillary. The electrocatalytic activity of the ink-modified electrodes toward the RRO was evaluated by cyclic voltammetry (CV) between 0 V and -1.0 V, and linear sweep voltammetry (LSV) between 0 V and -1.3 V. All the experiments were realized at a scan rate of 10 mV s^{-1} using 0.1 M KOH as electrolyte under saturated N_2 or O_2 atmosphere. Indeed, Goodenough et. al. [29] as well as other studies demonstrated the direct and efficient correlation between the features of OER and ORR tested under KOH alkaline conditions and those of OER and ORR tested under organic conditions [30,31]. LSV studies were performed at different rotation rates from 400 to 1600 rpm. RRDE measurements were performed for peroxide detection during the ORR process keeping the Pt ring at a fixed potential of E = 0.47V vs Ag/AgCl [32]. The collection efficiency (N) was determined as 0.23. The measured potential obtained versus Ag/AgCl was converted to the scale of reversible hydrogen electrode (RHE) through Equation 1:

$$E_{RHE} = E_{Ag/AgCl} + 0.199 + 0.059 \times pH \quad (1)$$

The fraction of peroxide generated by reduction of O_2 measured by the ring electrode and the corresponding number of transferred electrons (n_{e-}) during RRO were obtained by applying Equation 2 and 3, respectively: [33]

$$\% \boldsymbol{HO_2^-} = \frac{2I_R/N}{I_D+I_R/N} \quad (2)$$

$$\boldsymbol{n_{e-}} = \frac{4\,I_D}{I_D+I_R/N} \quad (3)$$

where I_R is the ring current, I_D is the disk current, and N is the Collection Efficiency.

On the other hand, the number of electrons transferred during the whole reaction can be determined by the Koutecky-Levich (Equation 4): [34]

$$\frac{1}{J} = \frac{1}{J_k} + \frac{1}{J_d=(0.62nFD_0^{2/3}v^{-1/6}C_0\omega^{1/2})} \quad (4)$$

where J is the total density of current measured, J_k is the kinetic density of current (A cm^{-2}), J_d is the diffusional density of current, n is the number of transferred electrons, F is the Faraday constant (96485 C mol^{-1}), D_O is the oxygen diffusion coefficient ($1.93 \cdot 10^{-5}$ cm^{-2} s^{-1}) , v is the kinematic viscosity of the electrolyte ($1.09 \cdot 10^{-2}$ cm^2 s^{-1}), C_O is the saturation concentration of O_2 in 0.1M KOH ($1.26 \cdot 10^{-6}$ mol cm^{-3}), and ω is the electrode rotation rate. From the slope of graph corresponding to J^{-1} vs $\omega^{-1/2}$, the number of electrons (n) involved in the whole reaction can be calculated.

The O_2 electrode was prepared as a coating layer over carbon paper gas-diffusion layer (GDL; SIGRACET GDL-24BC, SGL Technologies), consisting of a carbon paper and a microporous carbon layer with air permeability equal to 0.6 cm^3 cm^{-2} s^{-1} according to Sigraget data sheets. To prepare catalyzed cathodes, SnO_2@C45 was mixed with additional C45 ((TIMCAL C-NERGY TM Super C45-Imerys) to ensure good electronic conductivity, and PTFE binder (aqueous dispersion 60 wt%, ALDRICH), in the weight ratio of 25:65:10. Ethanol was added to the solid mixture to obtain a uniform slurry. The slurry was coated on the top of the microporous layer of the GDL using doctor blade technique. The thickness of the slurry deposited, including the solvent, was set at 200 μm. The as-prepared cathodes present a SnO_2

loading of 10 wt% of the total active material weight. As a mean of comparison, standard cathodes were prepared by mixing C45 with PTFE in the weight ratio 90:10. The slurry was obtained as described above and coated on GDL with a thickness of 200 μm.

For full-cell testing, discs with an area of 2.54 cm^2 were cut from the prepared coated GDL sheets, dried in vacuum at 120 °C for 6 h and used as a cathode. A Li disc (18 × 0.2 mm, Chemetall s.r.l) was used at the anode, a commercial disc of glass fiber (18 × 0.65 mm, ECC1-01-0012-A/L, EL-CELL) was used as the separator. 200 μL of the electrolyte solution consisting of LiTFSI 0.5 M in DMSO was added to the cells. The cells were assembled in an Ar-filled glove box (Mbraun Labstar) using an ECC-Air electrochemical cell design (EL-Cell, GmbH). They were galvanostatically discharged and charged by an Arbin BT-2000 battery tester at room temperature, between 2.0 and 4.5 V *vs.* Li^+/Li. During measurements, pure O_2 at a flow rate of 3.0 mL min^{-1} was constantly fluxed. Prior to each test, cells rested under oxygen flow for 6 h at open-circuit voltage (OCV).

To get the full-discharge/charge capacities of the different cathodes, the cells were galvanostatically discharged at room temperature, from the open circuit voltage (OCV) to 2.0 V *vs.* Li^+/Li at different current rates, and successively recharged to 4.5 V *vs.* Li^+/Li. To investigate the cycleability of the cells, galvanostatic time-controlled charge and discharge steps were carried out in the voltage range of 2.0–4.5 V *vs.* Li^+/Li. Resistivity of the cells in pristine state, after discharge and after recharge was investigated by EIS spectroscopy, in the frequency range 100 kHz - 1 Hz, at open circuit potential, using a CHI potentiostat instrument.

3. Results and discussion

The detailed mechanism involved in the formation of sub-5 nm SnO_2 nanoparticles spatially distributed on carbon black C-NERGY TM Super C45, was previously investigated and reported by our group [25]. In particular, the chosen strategy exploits the easy C45 hydrolysis as well as its specific surface chemistry (*i.e.* high concentration of oxygen functional groups) [35] as described hereafter. $SnCl_2•2H_2O$ was solubilized in distilled water, followed by the

addition of C45 to the colloidal suspension. At this point, thanks to electrostatic interactions with the negatively charged surface groups of C45, the positively charged $Sn(OH)^+$ species could easily be loaded on the carbon surface, where they experience hydrolysis:

$$Sn(OH)^+Cl^- (aq) + H_2O (l) \rightarrow Sn(OH)_2 (aq) + HCl$$

Successively, thanks to oxygen in air, tin (II) was oxidized to tin (IV), allowing for $Sn(OH)_2$ (aq) to self-evolve into ultra-small SnO_2 nanoparticles on the surface of C45 supplying nucleation sites for the deposition:

$$Sn(OH)_2 (aq) + ½O_2 (g) \rightarrow SnO_2 + H_2O$$

The morphology of the obtained composite material was assessed by FESEM and TEM analysis, the corresponding micrographs are reported on Figure 1. FESEM was also performed on commercial C45 for comparison. As can be seen on Figure 1a and b, C45 consists of slightly large primary particles, with average diameter between 40 and 60 nm, while the micrographs of SnO_2@C45 (Figure 1c and d) highlight the presence of SnO_2 nanoparticles homogeneously dispersed on the C45 surface. In particular, at higher magnification, the surface of pure C45 appears smoother (Figure 1 b) than the one of SnO_2@C45, because of the presence of SnO_2 nanoparticles (Figure 1 d). Indeed, the whole C45 surface seems to be homogeneously covered by SnO_2 nanoparticles with an average particle dimension around 5.0 nm. In order to verify the average diameter of SnO_2 nanoparticles, TEM was also performed, and the micrographs are reported on Figure e and f. Micrographs observation confirms the presence of small crystalline particles, around 5 nm, homogeneously distributed on the surface of C45, and some larger aggregates.

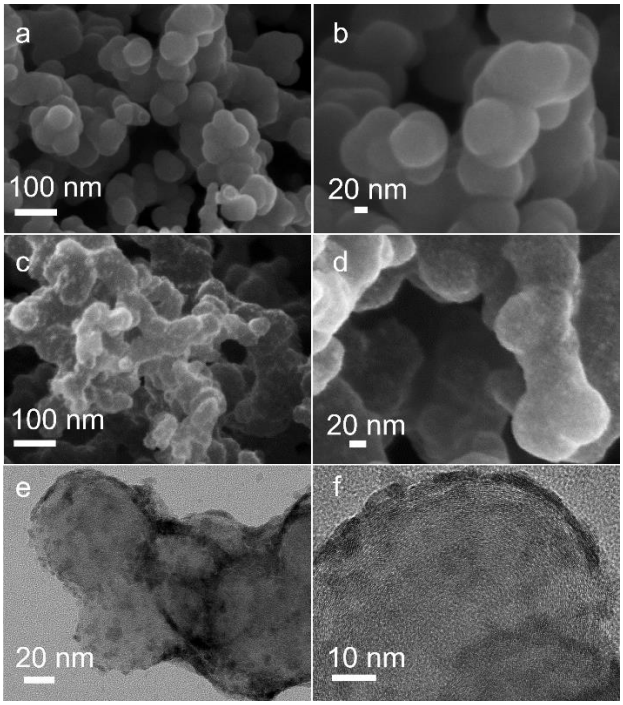

Figure 1 FESEM micrographs of C45 at low (a) and high (b) magnification, FESEM micrographs of SnO_2@C45 at low (c) and high (d) magnification, TEM analysis of SnO_2@C45 at low (e) and high (f) magnification.

In order to confirm that such crystalline phases belong to SnO_2 nanoparticles, XRD analysis was performed, and the results are reported on Figure S1. The C45 XRD spectrum shows two peaks at 25 °and 44 °, which are assigned to (002) and (101) graphitic planes, respectively [36]. Meanwhile, the SnO_2@C45 spectrum, shows three main broad peaks at 26.5 °, 33.9 °and 51.8 °, corresponding to the (110), (101) and (211) planes of rutile-tetragonal SnO_2 phase (JCPDS card No. 41-1445). The broader shape of the peak can be attributed to the SnO_2 small particle size [37].

In order to estimate the actual content of SnO_2 on C45, thermogravimetric analysis (TGA) was performed on SnO_2@C45 between 25 °C and 800 °C in air atmosphere, for comparison the analysis was performed, in the same conditions, on C45 sample (Figure S2). The SnO_2@C45 weight fluctuation in the temperature range of 25–200 °C can be attributed to water and gases absorbed from the ambient atmosphere, afterward the graph shows a small inflection after 500 °C due to the oxidation of residual stannous compounds. The most significant weight loss is observed between 500 and 600 °C and can be ascribed to the carbon combustion. Above

600 °C, the residual weight is attributed to SnO_2 and the corresponding mass percentage is 34 wt%. Interestingly, as we previously observed [25], on the pure C45 samples carbon combustion starts at higher temperature (around 650 °C) compared to the SnO_2@C45 sample, this can be explained by the catalytic effect known as Mars-van-Krevelen mechanism and further demonstrates the strong chemical interaction of SnO_2 and C45 in the prepared composite [38–41].

The performances of SnO_2@C45 nanocomposite and C45 as catalysts for the ORR were evaluated by cyclic voltammetry in 0.1 M KOH under N_2 and O_2 saturated solution, following the procedures reported by several studies and demonstrating the validity of the correlation between OER and ORR features tested in alkaline electrolytes and those obtained in aprotic electrolytes [29–31]. Figure 2a depicts the voltammetric profiles of both systems, showing that C45 and SnO_2@C45 are active for oxygen reduction. Both systems presented an intense current peak close to 0.6 V. This signal corresponds to the formation of peroxide [30] :

$$O_2 + H_2O + 2e^- \rightarrow HO_2^- + OH^- \text{ (I)}$$

The intensity of this signal, in terms of current, for C45 and SnO_2@C45, is practically the same, which allows us to infer that this peak is mainly associated with the oxygen reduction reaction on the active sites of the C45 material (which is in both systems in the same proportion). Then, as the potential sweep shifted toward negative values, only SnO_2@C45 nanocomposite presented a second reduction peak at ca. 0.1 V corresponding to the reduction of peroxide to water [30]:

$$HO_2^- + H_2O + 2e^- \rightarrow 3\,OH^- \text{ (II)}$$

This process, that was not detected for the C45 system, clearly shows the effect of SnO_2 in the SnO_2@C45 nanocomposite toward ORR. The profile of the system SnO_2@C45 corresponds to a global reduction of oxygen through a 2+2 electrons mechanism (I + II) giving as final product only water.

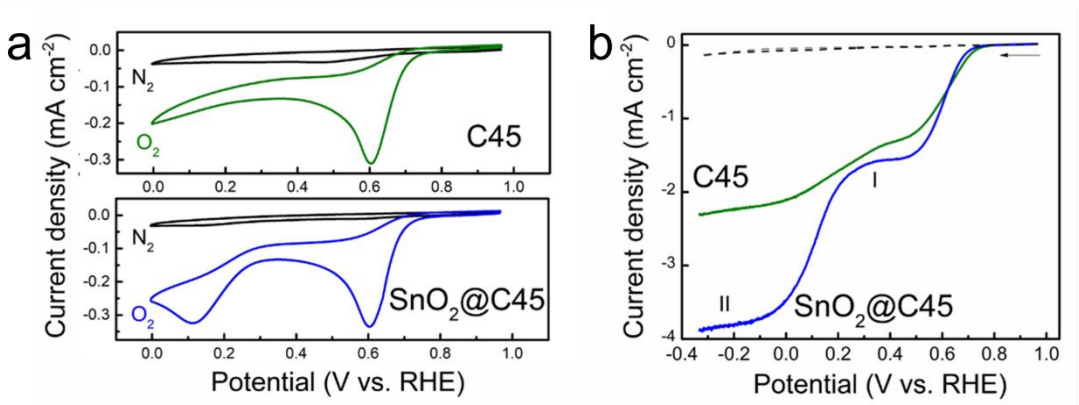

Figure 2 Cyclic voltammograms of C45 (green) and SnO_2@C45 (blue) catalysts in 0.1 M KOH solution in O_2 saturated and N_2 saturated at a scan rate of 10 mV s^{-1} (a). LSV profile for ORR of C45 and SnO_2@C45 catalysts at 1600 rpm rotation rate. Dotted line corresponding to response in N_2 saturated solutions for both electrodes (b).

Subsequently, ORR was studied using linear scanning voltammetry (LSV) with a rotating electrode to verify peak assignment and corresponding peroxide or water formation from profiles obtained by cyclic voltammetry. Figure 2b compares the responses of both electrodes at 600 rpm in the absence and presence of O_2. For C45, a signal is observed that begins to appear close to ~0.8 V, showing a slight reduction wave around 0.6 V, then presenting an increasing current until reaching a curve that tends to a plateau, that could be attributed to maximum diffusion limiting current density (2.4 mA cm^{-2}). For SnO_2@C45, a reduction wave is observed at potentials close to 0.6V followed by a small plateau (denoted in figure 2b as I) and then a marked increase in the current until reaching a second plateau (marked as II). For the first plateau, the current of the two systems is similar, indicating a first reduction process that occurs on an equivalent number of active sites. Then, for the SnO_2@C45 system, the second plateau reaches a current of 3.9 mA cm^{-2}, which corresponds to almost twice the current observed in the first plateau, showing that the incorporation of SnO_2 in the nanocomposite doubles the area available for the second reduction process. When comparing the onset potential of the ORR obtained for C45 and SnO_2@C45, it is observed that these values are practically the same (~0.8 V) but it is interesting to note that SnO_2@C45 indeed allows a second reduction process. These results are a first clue that would suggest that the oxygen reduction reaction for SnO_2@C45 could go through an initial hydroperoxide formation (signal I), widely reported in literature as

the 2 electrons transfer process [1,42], which lowers the overall OER reaction efficiency, degrading the active metal centers. Interestingly, this process is closely followed by a second reduction of the OH_2^- intermediate to OH^- (signal II) thus avoiding the formation and accumulation of harmful intermediates and guaranteeing high energy conversion efficiency.

In particular, in the SnO_2@C45 nanocomposite, C45 acts as an active site for the formation of HO_2^- and the SnO_2 nanoparticles for the formation of HO^- from HO_2^-, as described below:

$$C45 + O_2 \rightarrow C45/O_{2(ads)}$$

$$C45 - O_{2(ads)} + H_2O + 2e^- \rightarrow C45 + HO_2^- + OH^-$$

$$SnO_2 + HO_2^- \rightarrow SnO_2/HO_{2(ads)}^-$$

$$SnO_2/HO_{2(ads)}^- + H_2O + 2e^- \rightarrow 3\,OH^- + SnO_2$$

In order to confirm such catalytic pathway, the oxygen reduction process was monitored by linear sweep voltammetry technique, using a rotating ring disk electrode, applying a fixed potential to the ring to detect and quantify the formation of peroxide. These analyses were carried out at different rotational rates. The LSV profile obtained with the currents detected by the ring are presented for each system in Figure 3a and b. In both profiles, an increase in the limiting current was observed as the rate of rotation of the electrode increased, indicating that the electron transfer of the reaction is limited by diffusion. For C45, the oxygen reduction reaction begins at 0.80 V, and from this potential, peroxide begins to be detected in the ring, with an intensity directly correlated with the current observed in the disk. As the potential scan reaches more negative values, the detected current increases until it reaches a relatively constant value at 0 V. In the case of SnO_2@C45, the reduction begins at practically the same potential. However, zone I generates a considerable current in the ring until reaching a maximum value of 0.2 V, afterward the current detected by the ring drops to low current values in correspondence with zone II of the oxygen reduction process. This response confirms that the

second signal detected for SnO_2@C45 corresponds to an almost complete reduction of the hydrogen peroxide generated during the first process.

The percentage of peroxide generated was determined from the data obtained by LSV at 1600 rpm, together with the number of electrons for the different stages of the ORR (Figure 3c). In the case of C45, around 75% of peroxide was detected during the potential scan, with an average value of 2.5 electrons transferred. This value shows that for C45, the reduction process happens mainly through the 2 electrons transfer process, leading to peroxide as the majority product. In the case of SnO_2@C45, 78% of peroxide was detected at the beginning of the reaction, but as the scan shifted towards negative potentials, the percentage decreased until reaching a value below 15%, while the number of electrons transferred ranged between 2.4 at the beginning and 3.7 at the end. In this case, a strong dependence to the applied potential is observed. These values demonstrate a final reduction mechanism of 4 electrons transferred for SnO_2@C45, where the first stage is associated, as previously proposed, with a transfer of 2 electrons corresponding to the formation of peroxide, which then, in a second stage at more negative potentials, leads to an additional reduction via 2 electrons to form water.

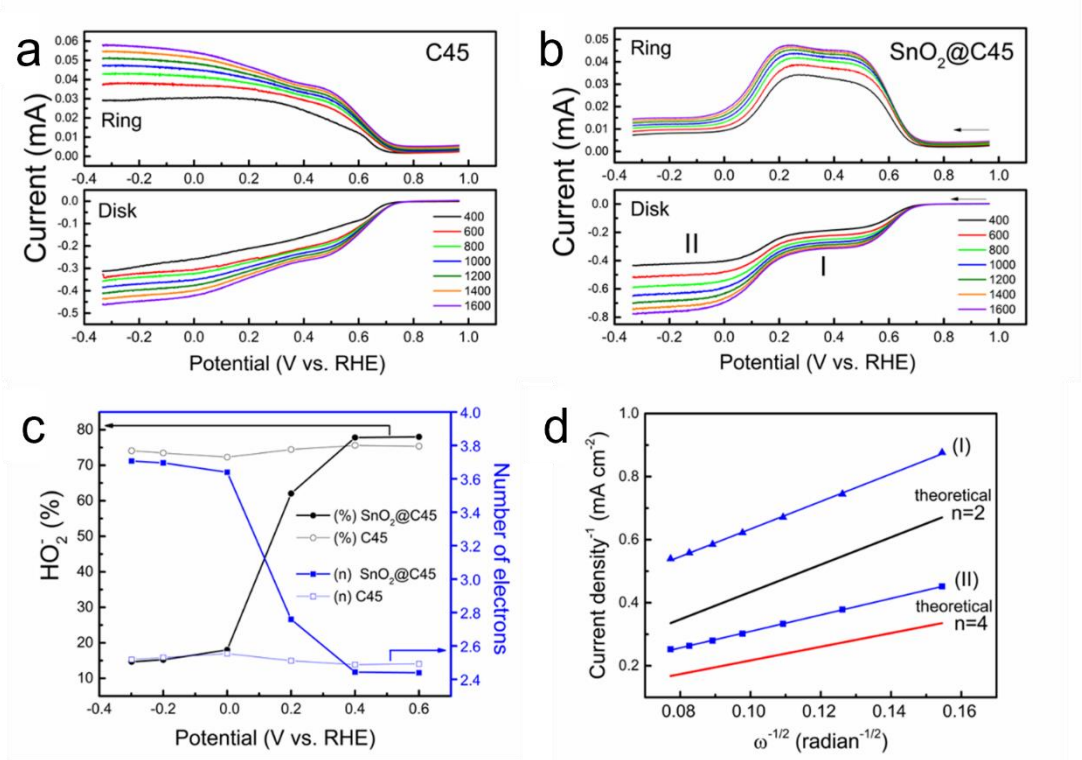

Figure 3 LSV profile recorder at different rotations using RRDE at a scan rate of 10 mVs-1, at a fixed potential of 0.47V (vs. Ag/AgCl) on the ring electrode. (a) C45 and (b) SnO_2C45. (c) Number of transferred electrons (n) and percentage of peroxide corresponding to C45 and SnO_2@C45 determined by RRDE at 1600 rpm (d) K-L graphs for SnO_2@C45 at 0.2V (I) and -0.3V (II) at different rotation rates.

To confirm the number of electrons involved for SnO_2@C45, the Koutecky-Levich (K-L) plot (Figure 3d) was constructed as the inverse of the current density (J^{-1}) as a function of the rotation of the electrode ($\omega^{-0.5}$) at the fixed potentials of -0.2 V and -0.3 V (potentials associated with processes I and II, respectively). For both processes, a linear relationship between J^{-1} and $\omega^{-0.5}$ was identified. On the other hand, the theoretical curves associated with a 2 and 4 electrons transfer were also plotted. It is clearly observed that, at the chosen potentials, two different trends are obtained. At -0.2V, the experimental line is parallel with the theoretical curve for n = 2. On the other hand, at -0.3 V, the experimental line is parallel to the theoretical curve n = 4. This further confirms the ORR route for the SnO_2@C45 is formed by two reduction processes, a first one, at lower potential, consisting in the reduction of oxygen to peroxide and then a second one, at a more negative potential, corresponding to the reduction of peroxide to water. In the SnO_2@C45 nanocomposite, the role of SnO_2 is therefore to promote the second reduction

process, resulting in the SnO_2@C45 nanocomposite reducing oxygen through a four-electron pathway (2 + 2 electrons) and avoiding the accumulation of peroxide, leading to sluggish ORR kinetics, and poor cells performances.

Furthermore, the linear portions of the polarization curves (Figure 2b) were fitted to the Tafel Equation (Equation 5). In particular, from LSV measurements (1600 rpm at 10 mV s^{-1}), in the low potential region, ranging from 0.77 to 0.70 V for SnO_2@C45 and 0.75 to 0.68 V for C45. The kinetic current, j_k, was calculated from the mass-transport correction of RDE using Equation 5, and then the Tafel slope (b) was obtained from Equation 6:

$$j_k = \frac{j \times j_L}{j_L - j} \qquad (5)$$

$$\eta = a + b \log j_k \qquad (6)$$

where η is the electrode overpotential, j_k is the kinetic current, and a and b are the Tafel intercept and Tafel slope, respectively. The Tafel slope is an intensive quantity depending on the reaction mechanism [16]. Indeed, the b value is strictly linked to the rate limiting step for ORR activity (see SI for more detail). The Tafel graphs (j_K vs. overpotential (V)) for each system are presented in Figure 4. The differences in the Tafel slope are not significant, and both show the same kinetic process. This process is associated with a chemical step, subsequent to the first charge transfer, as a rate-determining step (corresponding theoretically to a slope of 59mV/decade). This agrees with previous results, in that the role of SnO_2 is to be a catalyst for the second reduction observed in the system [20,43].

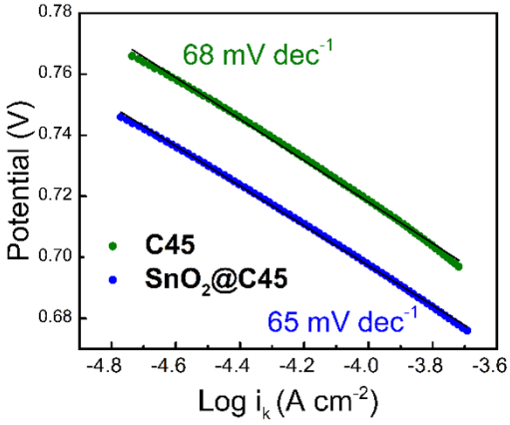

Figure 4 Tafel plots of C45 and SnO_2@C45 for the ORR.

The aforementioned catalytic activity of SnO_2@C45 is further demonstrated by assembling a full Li-O_2 cell, where the material is used at the cathode, over a gas diffusion layer, the electrolyte is a solution of 0.5 M LiTFSI in DMSO on a glass fiber separator, and the anode is a Li metal disc. As a mean of comparison, cells containing only C45 at the cathode are also assembled. For all electrochemical testing cells are constantly flowed with O_2 at 3 ml min^{-1}. Rate performances for C45 and SnO_2@C45 cells were measured, between 2.0 V and 4.5 V (vs. Li^+/Li) at various current densities from 0.1 mA cm^{-2} to 0.5 mA cm^{-2}, the results are reported on Figure 5. All the potential reported hereafter are intended *vs.* Li^+/Li.

The cell containing the SnO_2@C45 cathode shows a higher specific capacity than the one containing the C45 cathode, with respectively 9.6 mAh cm^{-2} and 6.9 mAh cm^{-2} at 0.1 mA cm^{-2}. Interestingly, the difference becomes much more obvious increasing the current density up to 0.5 mA cm^{-2}, with 6.5 mAh cm^{-2} against 2.3 mAh cm^{-2}, for SnO_2@C45 and C45 respectively. Indeed, the prime feature of a catalyst for this application would be to have better O_2 binding capacity, leading to higher ORR activity [42], this is quite obvious at the intermediate current density of 0.2 mA cm^{-2} where, in addition to the much higher specific capacity of SnO_2@C45 with 7.8 mAh cm^{-2} compared to the 3.2 mAh cm^{-2} of C45, the discharge plateau of the first cell is quite stable at around 2.75 V (vs. Li^+/Li) while the one of the second cell fluctuates around 2.62 V (vs. Li^+/Li), demonstrating a higher overpotential. As a matter of fact, in both cases,

with the increase in current density, the overpotential increases, however this increase is much more limited for the SnO_2@C45 cell compared to the C45 cell, which indicates that the composite cathode presents the lowest polarization and the highest energy conversion efficiency under increasing current densities [28].

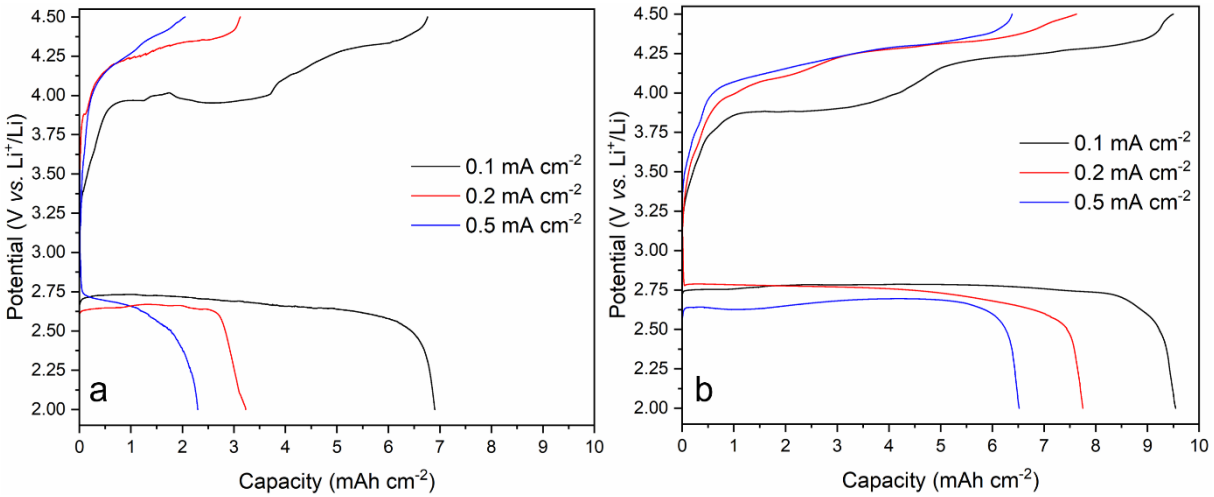

Figure 5 Discharge/charge cycles of the C45 cell (a) and the SnO_2@C45 (b) cell at different current densities with a discharge potential cut-off of 2.0 V and a charge potential cut-off of 4.5 V.

Ex situ analysis were conducted on cathodes, at different cycling steps to identify the discharge products, better assess their mechanism of formation and successive decomposition and their influence on cell performances. The steps considered are, a fresh cell, a cell discharged at 0.1 mA cm^{-2} until it reached the cut-off potential of 2.0 V, and a cell discharged in the previous conditions and recharged at 0.1 mA cm^{-2} until it reached the cut-off potential of 4.5 V (corresponding to the black voltage profiles reported on Figure 5a and b).

The first analysis carried out to this aim is EIS measurement, the corresponding Nyquist plots are reported on Figure 6a and b. Keeping in mind that the diameter of the semicircle corresponds to the charge transfer resistance (R_{ct}), the first observation is that R_{ct} increases significantly after discharge, for both cells, this is explained by the formation of the main discharge product for the Li-O_2 system, which is Li_2O_2 and is well known for its poor electron conductivity. Interestingly though, the corresponding R_{ct} value is smaller for the SnO_2@C45 cell (Figure 6b) compared to the C45 cell (Figure 6a), indicating a more efficient electrons/charge transfer at

the surface of the catalyzed cathode even after Li_2O_2 formation [16]. After recharge, the R_{ct} of the SnO_2@C45 cell closely recovers its initial value, indicating the complete decomposition of the discharge products previously formed. Conversely, for the C45 cell, R_{ct} is much higher than the one of the fresh cell. This can be explained by an incomplete decomposition of the discharge products previously formed, in addition to the fact that such discharge products may not be exclusively composed of Li_2O_2 [20]. In order to identify these discharge products, XRD measurements were performed on the corresponding cathodes and the results are reported on Figure 6c and d. As a mean of comparison XRD was also performed on a pristine GDL foil, used as support for the studied electrodes, to be able to discriminate its contribution in the different spectra. The XRD patterns of both discharged cathodes present peaks at 32.5°,35.9°, and 51.5° corresponding to the (100), (101), and (103) crystal planes of Li_2O_2, the expected discharge product of Li-O_2 cells [21]. Additional peaks are present at 21.4° and 36.6° corresponding to crystal planes of Li_2CO_3 which formation is usually explained by super-oxygen ion nucleophilic attack and consequent electrolyte decomposition [44]. The last two peaks, at 20.3° and 62.2° can be ascribed to LiOH formation, previously reported as a possible product of either binder decomposition upon cycling [45] or DMSO after long exposure to Li_2O_2 [11]. Interestingly, observing Figure 6d it is possible to see how the intensity of the previously described peaks is lower compared to the spectrum of Figure 6c, corresponding to the C45 cell. Two hypotheses can be proposed regarding this observation, either the quantity of such discharge products is lower, or their crystallinity is lower, though the higher discharge capacity of the SnO_2@C45 cathode observed in Figure 5b would tend to invalidate the first hypothesis. The corresponding spectrum after recharge demonstrates the complete disappearance of the previously described peaks on the SnO_2@C45 cathode, confirming the excellent reversibility of the discharge products previously formed [21], while for the C45 cathode, only the peaks corresponding to Li_2O_2 completely disappear after recharge, meaning that Li_2CO_3 and LiOH are not completely decomposed. This probably can be explained by the

poor interaction between C45 and the discharge products, resulting in a certain amount of residual substances on the cathode after the recharge process and their subsequent accumulation upon cycling. Such results confirm the previous EIS analysis and reveals that the presence of SnO_2@C45 can indeed facilitate charge transfer and avoid the large interface resistance caused by the generation of insoluble discharge products [44].

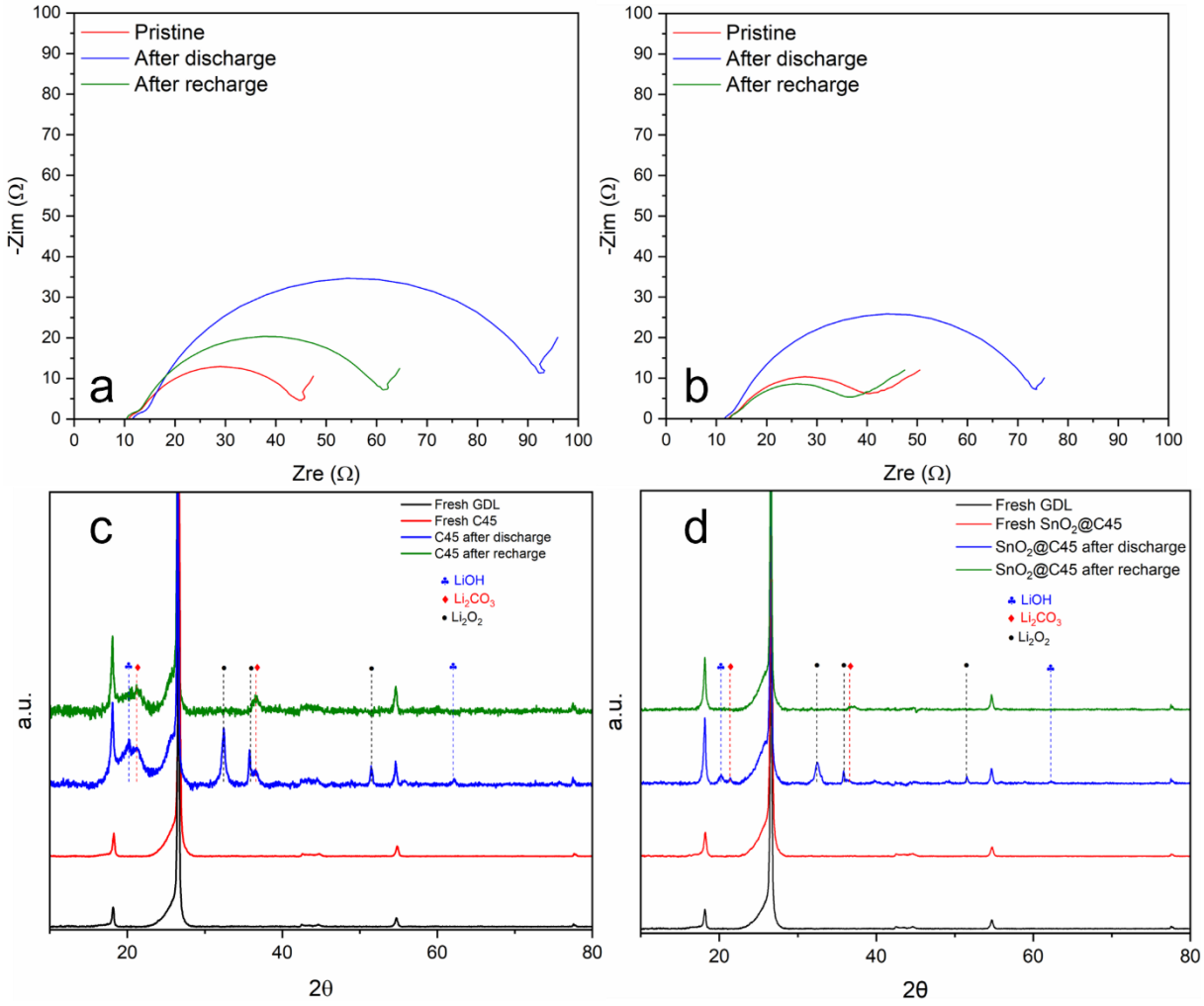

Figure 6 EIS of the C45 cell (a) and the SnO_2@C45 cell (b) at different cycling steps at 0.1 mA cm^{-2}, XRD of the corresponding C45 (c) and SnO_2@C45 (d).

To observe the morphology of the discharge products previously identified and described, FESEM analysis was carried out on the same cathodes, the corresponding micrographs are reported on Figure 7.

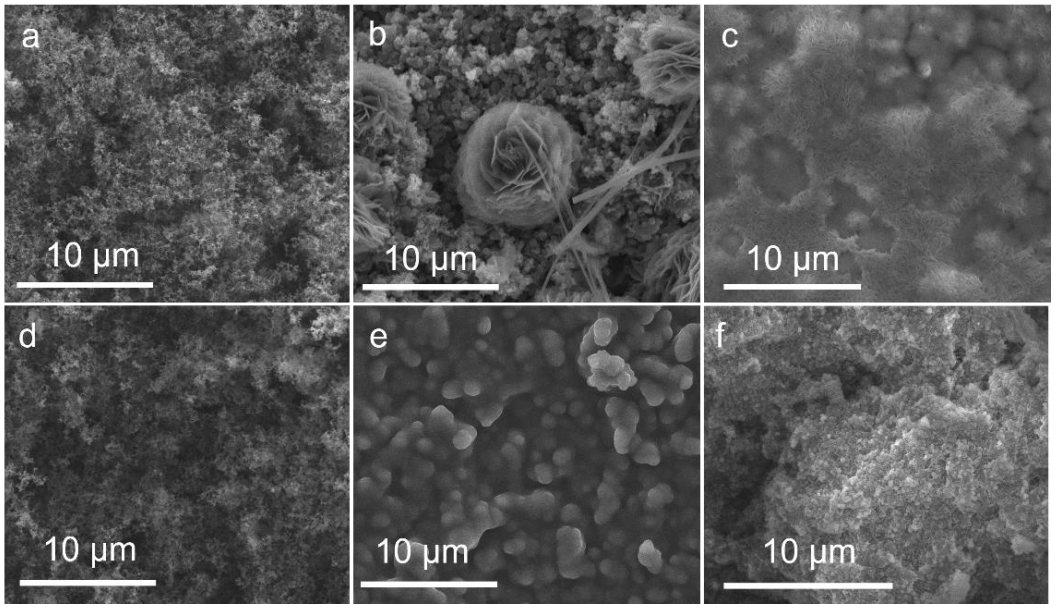

Figure 7 FESEM micrographs of pristine C45 (a) and SnO_2@C45 (d), discharged C45 (b) and SnO_2@C45 (e), recharged C45 (c) and SnO_2@C45 (f) cathode surfaces at 0.1 mA cm^{-2}

In the fresh state C45 (Figure 7a) and SnO_2@C45 (Figure 7d) cathodes surfaces present very similar morphologies, characterized by C45 nanoparticles homogeneously distributed, on the surface, SnO_2 nanoparticles are actually too small to be seen on such micrographs. On the contrary, after discharge, the surface morphologies of both cathodes are drastically different. As can be seen on Figure 7b (and Figure S3a) on the surface of C45 cathode, Li_2O_2 is formed in the widely reported micrometric toroidal shape [12,15]. Such toroids present large dimensions and seem homogeneously distributed on the whole cathode surface (see Figure S3a). On the other hand, no toroids can be seen on the surface of SnO_2@C45 cathode, which seems to be entirely covered by an amorphous film (see Figure 7e and Figure S3c) quite similar to the morphology obtained in other papers [46,47]. As a matter of fact, previous studies demonstrated that the typical $Li-O_2$ intermediate discharge product, LiO_2, is less stable on several rutile (e.g. RuO_2, TiO_2 and SnO_2) or tailored carbon nanotubes surfaces, and are therefore further reduced to Li_2O_2 through disproportionation reaction. For the first and second layers of Li_2O_2 deposited, the adsorption energy is comparable to the bulk Li_2O_2 cohesive energy, thus justifying the oxide surfaces wetting by Li_2O_2 and its growing into thin films rather than particles. In particular, electronic structure analyses of Li_2O_2/SnO_2 interface demonstrated its semiconducting

character, with a bandgap of 0.2 eV, therefore noticeably lower than the one of bulk Li_2O_2. Hence, amorphousness of Li_2O_2 is probably due to the large lattice mismatch at these interfaces, thus forming film-like morphology [44,48,49]. Several recent works reported the advantages of film-like discharge products upon other morphologies such as bead-type particles, mesh-like fibers or toroids [22,44,50,51]. Indeed, the film-like morphology efficiently increases the contact area between the cathode surface and the discharge product and therefore significantly enhances the electrons transfer, thus resulting in a reduced overvoltage upon cycling. Observing the morphologies of the 2 cathodes after recharge, it can be noted that C45 cathode (Figure 7c and Figure S3b) remains covered with partially decomposed products and does not recover its initial structure. In the meantime, the morphology of the SnO_2@C45 (Figure 7f and Figure S3d) looks very similar to the one of the fresh cathode, demonstrating the complete decomposition and the good reversibility of the obtained amorphous discharge product, in accordance with the XRD analysis.

Further, to precisely verify the catalyst role and its stability upon cycling, galvanostatic charge-discharge of the full Li-O_2 cell was performed at a current density of 0.5 mA cm^{-2} and with limited capacity of 1 mAh cm^{-2} such a short discharge/charge time was selected in order to avoid interferences caused by non-catalyst factors, such as decomposition of electrolyte, Li dendrites growth, and irreversible formation of other byproducts, the obtained results are reported in Figure 8.

Observing the cycling profiles of the C45 and SnO_2@C45 (Figure 8a and b) they seem quite similar for the first cycles. However, calculating the overpotential, as the difference between charge and discharge potential at the fixed capacity of 0.5 mAh cm^{-2}, the air cathode behavior can be more deeply investigated. As can be seen on Figure 8d, after an initial decrease for the first 30 cycles, the overpotential of the C45 cell shows a steep increase after the 30^{th} cycle and fails after the 40^{th} cycle (see detail on Figure S4). On the other hand, the cell containing the SnO_2@C45 cathode can stably run for more than 70 cycles with limited overpotential variation.

Therefore, even at a high current density of 0.5 mA cm^{-2} the catalyzed cathode exhibits lower overpotential than the C45 cell, indicating the excellent reversibility and cycling stability of the composite material. Such a reduced overpotential can be ascribed to the catalytic activity of SnO_2@C45, promoting the adsorption O_2 and discharge products, as well as efficient electron transfer favored by their film-like morphology [44].

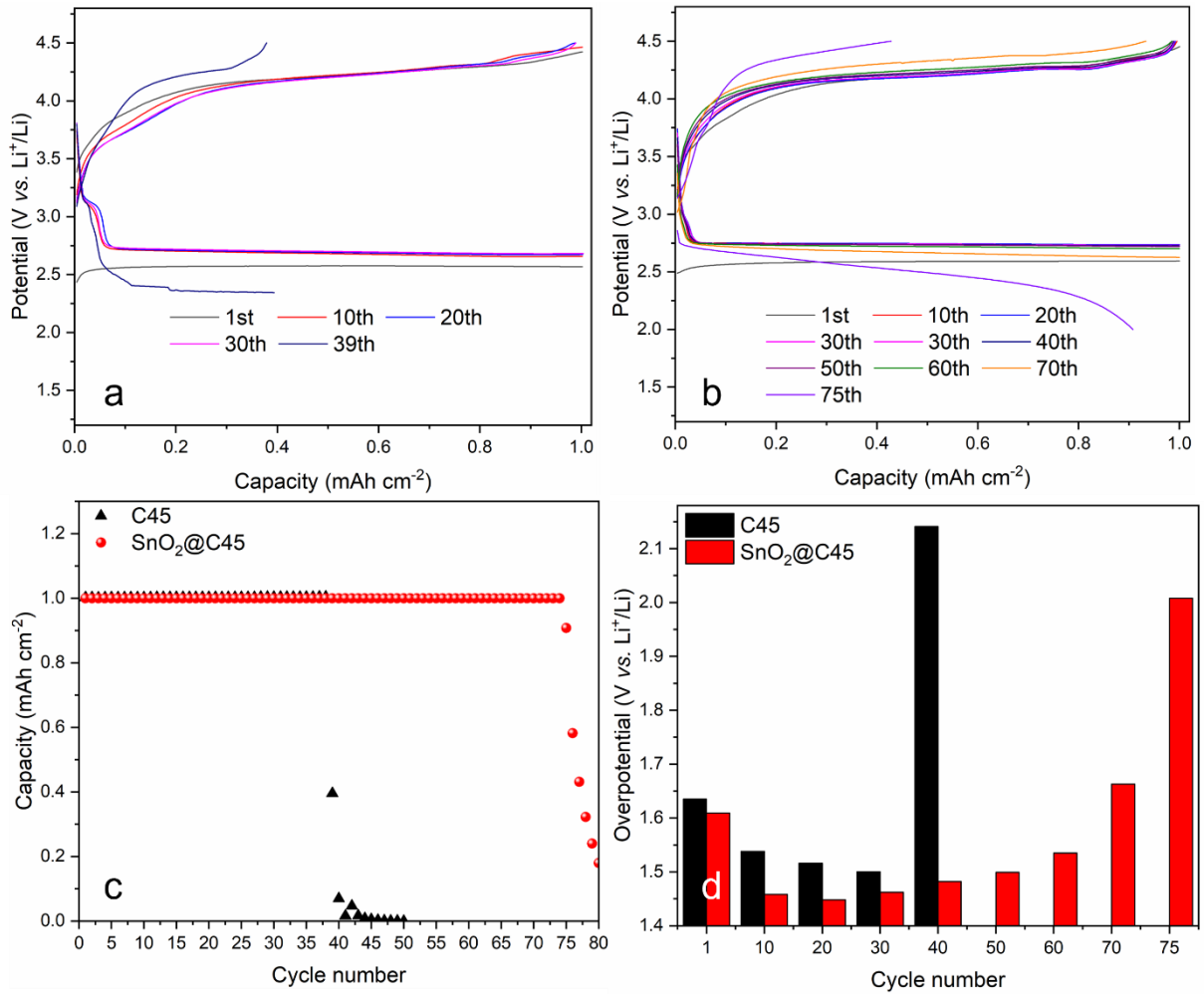

Figure 8 Cells performances at 0.5 mA cm^{-2} at fixed capacity of 1 mAh cm^{-2}: discharge/charge cycles of the C45 cell (a) and the SnO_2@C45 cell (b), discharge capacity comparison (c), overvoltage of both cells measured as the difference between charge and discharge potential at the fixed capacity 0.5 mAh cm^{-2} (d).

To further study the stability of SnO_2@C45 in more drastic conditions, additional galvanostatic cycling were performed at a current density of 0.1 mA cm^{-2} and a fixed capacity of 2.5 mA cm^{-2}, corresponding to 25 h of discharge/charge respectively. Such parameters were defined to assess the SnO_2@C45 behavior in conditions favoring parasitic reactions such as carbon and

electrolyte decomposition. The obtained results are reported on Figure S5. Observing Figures S5a and b, one of the first difference that can be noted compared to Figure 8a and b, is the presence of a second charge plateau around 4,2 V, for both SnO_2@C45 and C45 cell. According to the literature such plateau is typical of Li_2CO_3 decomposition [8,48]. Nevertheless, the SnO_2@C45 cell always shows a reduced overvoltage compared to the C45 cell (Figure S5d), demonstrating an improved cycling stability. Therefore, even if the presence of SnO_2@C45 in such drastic conditions does not completely block electrolyte decomposition, and the byproduct Li_2CO_3 is gradually accumulated on the composite cathode surface, such phenomenon is clearly limited by the presence of the composite air cathode compared to the C45 cell, with 27 cycles for the first one against 20 for the second one, which represents an additional cycle life of 350h (see Figure S5c) and therefore a noticeable increase of the energy efficiency. Such good performances obtained both at high current density and with long discharge/charge process represents an interesting progress compared to recently reported catalyst for Li-O_2 technology (See Table S1).

A hypothesis about the discharge mechanism on the SnO_2@C45 cathode can be proposed combining the here-discussed results and previous DFT studies [8], demonstrating that the adsorption energy of oxygen for SnO_2 is at least −2.74 eV, which is much higher than common carbon materials. Indeed, thanks to SnO_2 nanoparticles grafting onto C45, O_2 should be easily adsorbed on the catalyzed cathode during the cell discharge, followed by an electron addition, generating the surface adsorbed LiO_2*. Afterward, LiO_2* probably drives the nanosized Li_2O_2 growth on the cathode surface via “surface-adsorption pathway”, thus contributing to a relatively low overpotential. This is also confirmed by theoretical calculations demonstrating that the initial deposition of Li_2O_2 on the surface of SnO_2 could wet the active surface of SnO_2 and thus tend to generate a film-like morphology [49], which has been demonstrated to be far easier to decompose upon recharge thanks to a higher number of structural defects favorable to

charge transport and beneficial to electrooxidation [52], thus allowing for higher cell performances either at high current density or for long discharge/charge processes.

4. Conclusion

In summary, an efficient ORR catalyst was obtained through a facile and low-cost production strategy. Indeed, SnO_2 nanoparticles with an average size of 5.0 nm immobilized over the surface of commercial C-NERGY super C45 carbon black were easily obtained, since the C45 supplies nucleation sites for the deposition of SnO_2 and assists in chemically anchoring SnO_2 NPs. This way SnO_2 NPs are finely dispersed within the carbon host, offering a large number of active sites available for adsorbing O_2 and discharge products upon Li-O_2 cell cycling. As a matter of fact, ex-situ analyses demonstrated that the presence of SnO_2@C45 on the air cathode surface favored the formation of film-like morphology of the discharge products, thus allowing their easier decomposition upon recharge. This behavior allowed for a prolonged cycle life both at the high current density of 0.5 mA cm^{-2} and at a fixed capacity as high as 2.5 mAh cm^{-2}, thus overcoming recently reported performances of much more complicated and expensive catalysts. Moreover, the simple, sustainable and easily up-scalable process makes SnO_2@C45 a versatile material suitable for various energy storage applications.

Acknowledgements

This work was funded by "Accordo di Programma Ministero dello Sviluppo Economico-ENEA: Ricerca sul sistema energetico (RSE)", 2019–2021 (MISE ENEA); ANID, Convocatoria Nacional Subvención A Instalación En La Academia convocatoria año 2021 [grant number 77210080]; and Dicyt-Usach.

References

[1] S. Wu, D. Wu, D. Zhang, W. Liu, H. Luo, J. He, Q. Yang, Z. Li, R. Liu, Boosting the Activity and Stability with Dual-Metal-N Couplings for Li–O 2 Battery, ENERGY

Environ. Mater. n/a (2021) eem2.12210. https://doi.org/10.1002/eem2.12210.

[2] G. Ganas, G. Kastrinaki, D. Zarvalis, G. Karagiannakis, A.G. Konstandopoulos, D. Versaci, S. Bodoardo, Synthesis and characterization of LNMO cathode materials for lithium-ion batteries, Mater. Today Proc. 5 (2018) 27416–27424. https://doi.org/10.1016/j.matpr.2018.09.059.

[3] J. Amici, M. Alidoost, F. Caldera, D. Versaci, U. Zubair, F. Trotta, C. Francia, S. Bodoardo, PEEK-WC/Nanosponge Membranes for Lithium-Anode Protection in Rechargeable Li−O 2 Batteries, ChemElectroChem. 5 (2018) 1599–1605. https://doi.org/10.1002/celc.201800241.

[4] X.-Q. Zhang, X.-B. Cheng, Q. Zhang, Advances in Interfaces between Li Metal Anode and Electrolyte, Adv. Mater. Interfaces. 5 (2018) 1701097. https://doi.org/10.1002/admi.201701097.

[5] P.G. Bruce, S.A. Freunberger, L.J. Hardwick, J.-M. Tarascon, Li–O2 and Li–S batteries with high energy storage, Nat. Mater. 11 (2012) 19–29. https://doi.org/10.1038/nmat3191.

[6] B. Dunn, H. Kamath, J.-M. Tarascon, Electrical energy storage for the grid: a battery of choices., Science. 334 (2011) 928–35. https://doi.org/10.1126/science.1212741.

[7] D. Mei, X. Yuan, Z. Ma, P. Wei, X. Yu, J. Yang, Z.-F. Ma, A SnO 2 -Based Cathode Catalyst for Lithium-Air Batteries, ACS Appl. Mater. Interfaces. 8 (2016) 12804–12811. https://doi.org/10.1021/acsami.6b02402.

[8] J. Fu, X. Guo, H. Huo, Y. Chen, T. Zhang, Easily Decomposed Discharge Products Induced by Cathode Construction for Highly Energy-Efficient Lithium–Oxygen Batteries, ACS Appl. Mater. Interfaces. 11 (2019) 14803–14809. https://doi.org/10.1021/acsami.9b01673.

[9] B.D. McCloskey, R. Scheffler, A. Speidel, G. Girishkumar, A.C. Luntz, On the Mechanism of Nonaqueous Li–O 2 Electrochemistry on C and Its Kinetic

Overpotentials: Some Implications for Li–Air Batteries, J. Phys. Chem. C. 116 (2012) 23897–23905. https://doi.org/10.1021/jp306680f.

[10] K.H. Park, D.Y. Kim, J.Y. Kim, M. Kim, G.-T. Yun, Y. Kim, H. Joo, S. Choi, J. Suk, Y. Kang, M. Wu, W.-B. Jung, H.-T. Jung, Fabrication of Highly Monodisperse and Small-Grain Platinum Hole–Cylinder Nanoparticles as a Cathode Catalyst for Li–O 2 Batteries, ACS Appl. Energy Mater. 4 (2021) 2514–2521. https://doi.org/10.1021/acsaem.0c03082.

[11] S. Vankova, C. Francia, J. Amici, J. Zeng, S. Bodoardo, N. Penazzi, G. Collins, H. Geaney, C. O'Dwyer, Influence of Binders and Solvents on Stability of Ru/RuO x Nanoparticles on ITO Nanocrystals as Li-O 2 Battery Cathodes, ChemSusChem. 10 (2017) 575–586. https://doi.org/10.1002/cssc.201601301.

[12] S. Martinez Crespiera, D. Amantia, E. Knipping, C. Aucher, L. Aubouy, J. Amici, J. Zeng, C. Francia, S. Bodoardo, Electrospun Pd-doped mesoporous carbon nano fibres as catalysts for rechargeable Li–O 2 batteries, RSC Adv. 6 (2016) 57335–57345. https://doi.org/10.1039/C6RA09721A.

[13] E. Yilmaz, C. Yogi, K. Yamanaka, T. Ohta, H.R. Byon, Promoting Formation of Noncrystalline Li 2 O 2 in the Li–O 2 Battery with RuO 2 Nanoparticles, Nano Lett. 13 (2013) 4679–4684. https://doi.org/10.1021/nl4020952.

[14] Y. Kim, J.H. Park, J.G. Kim, Y. Noh, Y. Kim, H. Han, W.B. Kim, Ruthenium Oxide Incorporated One-Dimensional Cobalt Oxide Composite Nanowires as Lithium-Oxygen Battery Cathode Catalysts, ChemCatChem. 9 (2017) 3554–3562. https://doi.org/10.1002/cctc.201700560.

[15] S. Martinez Crespiera, D. Amantia, E. Knipping, C. Aucher, L. Aubouy, J. Amici, J. Zeng, U. Zubair, C. Francia, S. Bodoardo, Cobalt-doped mesoporous carbon nanofibres as free-standing cathodes for lithium–oxygen batteries, J. Appl. Electrochem. 47 (2017) 497–506. https://doi.org/10.1007/s10800-016-1035-0.

[16] C. Tomon, A. Krittayavathananon, S. Sarawutanukul, S. Duangdangchote, N. Phattharasupakun, K. Homlamai, M. Sawangphruk, Enhancing bifunctional electrocatalysts of hollow Co3O4 nanorods with oxygen vacancies towards ORR and OER for Li–O2 batteries, Electrochim. Acta. 367 (2021) 137490. https://doi.org/10.1016/j.electacta.2020.137490.

[17] L. Ren, R. Zheng, D. Du, Y. Yan, M. He, Z. Ran, M. Li, C. Shu, Optimized orbital occupancy of transition metal in spinel Ni-Co oxides with heteroatom doping for Aprotic Li-O2 battery, Chem. Eng. J. 430 (2022) 132977. https://doi.org/10.1016/j.cej.2021.132977.

[18] M. Yuan, Z. Sun, Z. Wu, D. Wang, H. Yang, C. Nan, H. Li, W. Zhang, G. Sun, Tuning the oxygen vacancy of mixed multiple oxidation states nanowires for improving Li-air battery performance, J. Colloid Interface Sci. 608 (2022) 1384–1392. https://doi.org/10.1016/j.jcis.2021.10.104.

[19] J.G. Kim, Y. Noh, Y. Kim, S. Lee, W.B. Kim, Fabrication of three-dimensional ordered macroporous spinel CoFe 2 O 4 as efficient bifunctional catalysts for the positive electrode of lithium–oxygen batteries, Nanoscale. 9 (2017) 5119–5128. https://doi.org/10.1039/C7NR00052A.

[20] X. Fan, Y. Huang, H. Wang, F. Zheng, C. Tan, Y. Li, X. Lu, Z. Ma, Q. Li, Efficacious nitrogen introduction into MoS2 as bifunctional electrocatalysts for long-life Li-O2 batteries, Electrochim. Acta. 369 (2021) 137653. https://doi.org/10.1016/j.electacta.2020.137653.

[21] A. Kondori, Z. Jiang, M. Esmaeilirad, M. Tamadoni Saray, A. Kakekhani, K. Kucuk, P. Navarro Munoz Delgado, S. Maghsoudipour, J. Hayes, C.S. Johnson, C.U. Segre, R. Shahbazian-Yassar, A.M. Rappe, M. Asadi, Kinetically Stable Oxide Overlayers on Mo 3 P Nanoparticles Enabling Lithium–Air Batteries with Low Overpotentials and Long Cycle Life, Adv. Mater. 32 (2020) 2004028.

https://doi.org/10.1002/adma.202004028.

[22] W. Jiao, Q. Su, J. Ge, S. Dong, D. Wang, M. Zhang, S. Ding, G. Du, B. Xu, Mo2C quantum dots decorated ultrathin carbon nanosheets self-assembled into nanoflowers toward highly catalytic cathodes for Li-O2 batteries, Mater. Res. Bull. 133 (2021) 111020. https://doi.org/10.1016/j.materresbull.2020.111020.

[23] A. Kolmakov, D.O. Klenov, Y. Lilach, S. Stemmer, M. Moskovits, Enhanced Gas Sensing by Individual SnO 2 Nanowires and Nanobelts Functionalized with Pd Catalyst Particles, Nano Lett. 5 (2005) 667–673. https://doi.org/10.1021/nl050082v.

[24] D. Versaci, J. Amici, C. Francia, S. Bodoardo, Simple approach using g-C3N4 to enable SnO2 anode high rate performance for Li ion battery, Solid State Ionics. 346 (2020) 115210. https://doi.org/10.1016/j.ssi.2019.115210.

[25] D. Versaci, A. Costanzo, S.M. Ronchetti, B. Onida, J. Amici, C. Francia, S. Bodoardo, Ultrasmall SnO2 directly grown on commercial C45 carbon as lithium-ion battery anodes for long cycling performance, Electrochim. Acta. 367 (2021) 137489. https://doi.org/10.1016/j.electacta.2020.137489.

[26] S.M. Hwang, Y.-G. Lim, J.-G. Kim, Y.-U. Heo, J.H. Lim, Y. Yamauchi, M.-S. Park, Y.-J. Kim, S.X. Dou, J.H. Kim, A case study on fibrous porous SnO 2 anode for robust, high-capacity lithium-ion batteries, Nano Energy. 10 (2014) 53–62. https://doi.org/10.1016/j.nanoen.2014.08.020.

[27] Y. Lee, H. Park, The Electrochemical Properties of SnO 2 as Cathodes for Lithium Air Batteries, J. Korean Electrochem. Soc. 22 (2019) 164–171. https://doi.org/10.5229/JKES.2019.22.4.164.

[28] J. Li, X. Hou, Y. Mao, C. Lai, X. Yuan, Enhanced Performance of Aprotic Electrolyte Li–O 2 Batteries with SnS 2 –SnO 2 /C Heterostructure as Efficient Cathode Catalyst, Energy & Fuels. 34 (2020) 14995–15003. https://doi.org/10.1021/acs.energyfuels.0c02877.

[29] Z. Du, P. Yang, L. Wang, Y. Lu, J.B. Goodenough, J. Zhang, D. Zhang, Electrocatalytic performances of LaNi1−Mg O3 perovskite oxides as bi-functional catalysts for lithium air batteries, J. Power Sources. 265 (2014) 91–96. https://doi.org/10.1016/j.jpowsour.2014.04.096.

[30] M. Liu, L. Wang, K. Zhao, S. Shi, Q. Shao, L. Zhang, X. Sun, Y. Zhao, J. Zhang, Atomically dispersed metal catalysts for the oxygen reduction reaction: synthesis, characterization, reaction mechanisms and electrochemical energy applications, Energy Environ. Sci. 12 (2019) 2890–2923. https://doi.org/10.1039/C9EE01722D.

[31] Y. Zhao, L. Xu, L. Mai, C. Han, Q. An, X. Xu, X. Liu, Q. Zhang, Hierarchical mesoporous perovskite La 0 .5 Sr 0.5 CoO 2.91 nanowires with ultrahigh capacity for Li-air batteries, Proc. Natl. Acad. Sci. 109 (2012) 19569–19574. https://doi.org/10.1073/pnas.1210315109.

[32] J. Sunarso, A.A.J. Torriero, W. Zhou, P.C. Howlett, M. Forsyth, Oxygen Reduction Reaction Activity of La-Based Perovskite Oxides in Alkaline Medium: A Thin-Film Rotating Ring-Disk Electrode Study, J. Phys. Chem. C. 116 (2012) 5827–5834. https://doi.org/10.1021/jp211946n.

[33] X. Ge, A. Sumboja, D. Wuu, T. An, B. Li, F.W.T. Goh, T.S.A. Hor, Y. Zong, Z. Liu, Oxygen Reduction in Alkaline Media: From Mechanisms to Recent Advances of Catalysts, ACS Catal. 5 (2015) 4643–4667. https://doi.org/10.1021/acscatal.5b00524.

[34] X. Min, Y. Chen, M.W. Kanan, Alkaline O 2 reduction on oxide-derived Au: high activity and 4e − selectivity without (100) facets, Phys. Chem. Chem. Phys. 16 (2014) 13601–13604. https://doi.org/10.1039/C4CP01337A.

[35] M.E. Spahr, D. Goers, A. Leone, S. Stallone, E. Grivei, Development of carbon conductive additives for advanced lithium ion batteries, J. Power Sources. 196 (2011) 3404–3413. https://doi.org/10.1016/j.jpowsour.2010.07.002.

[36] T. Jiang, A Comparative Study of Carbon Anodes Produced by Ball Milling for

Lithium-Ion Batteries, Juniper Online J. Mater. Sci. 1 (2017). https://doi.org/10.19080/JOJMS.2017.01.555562.

[37] P. Scherrer, Bestimmung der inneren Struktur und der Größe von Kolloidteilchen mittels Röntgenstrahlen, in: R. Zsigmondy (Ed.), Kolloidchem. Ein Lehrb., Springer Berlin Heidelberg, Berlin, Heidelberg, 1912: pp. 387–409. https://doi.org/10.1007/978-3-662-33915-2_7.

[38] K. Kisu, M. Iijima, E. Iwama, M. Saito, Y. Orikasa, W. Naoi, K. Naoi, The origin of anomalous large reversible capacity for SnO 2 conversion reaction, J. Mater. Chem. A. 2 (2014) 13058–13068. https://doi.org/10.1039/C4TA01994F.

[39] P. Mars, D.W. van Krevelen, Oxidations carried out by means of vanadium oxide catalysts, Chem. Eng. Sci. 3 (1954) 41–59. https://doi.org/10.1016/S0009-2509(54)80005-4.

[40] S. Aksel, D. Eder, Catalytic effect of metal oxides on the oxidation resistance in carbon nanotube–inorganic hybrids, J. Mater. Chem. 20 (2010) 9149. https://doi.org/10.1039/c0jm01129k.

[41] M. Dimitrov, T. Tsoncheva, S. Shao, R. Köhn, Novel preparation of nanosized mesoporous SnO2 powders: Physicochemical and catalytic properties, Appl. Catal. B Environ. 94 (2010) 158–165. https://doi.org/10.1016/j.apcatb.2009.11.004.

[42] M. Athika, V.S. Devi, P. Elumalai, Cauliflower-Like Hierarchical Porous Nickel/Nickel Ferrite/Carbon Composite as Superior Bifunctional Catalyst for Lithium-Air Battery, ChemistrySelect. 5 (2020) 3529–3538. https://doi.org/10.1002/slct.202000013.

[43] S. Pérez-Rodríguez, D. Sebastián, C. Alegre, T. Tsoncheva, N. Petrov, D. Paneva, M.J. Lázaro, D. Li, Q. Zhang, Z. Shen, K. Siddharth, L. Chen, M. Shao, Z. Shi, Y.F.Y. Wang, L.N. Song, Y.F.Y. Wang, F. Li, X.X. Wang, H.H.F. Wang, J.J. Xu, C. Zhao, C. Shu, R. Zheng, D. Du, L. Ren, M. He, R. Li, H. Xu, X. Wen, J. Long, S. Wu, D. Wu,

D. Zhang, W. Liu, H. Luo, J. He, Q. Yang, Z. Li, R. Liu, M. Athika, V.S. Devi, P. Elumalai, X. Fan, Y. Huang, H.H.F. Wang, F. Zheng, C. Tan, Y. Li, X. Lu, Z. Ma, Q. Li, K.H. Park, D.Y. Kim, J.Y. Kim, M. Kim, G. Yun, Y. Kim, D. Li, J. Liang, S.J. Robertson, Y. Chen, N. Wang, M. Shao, Z. Shi, Biomass waste-derived nitrogen and iron co-doped nanoporous carbons as electrocatalysts for the oxygen reduction reaction, Electrochim. Acta. 387 (2022) 138490. https://doi.org/10.1016/j.electacta.2021.138490.

[44] Y. Li, R. Zhang, B. Chen, N. Wang, J. Sha, L. Ma, D. Zhao, E. Liu, S. Zhu, C. Shi, N. Zhao, Induced construction of large-area amorphous Li2O2 film via elemental co-doping and spatial confinement to achieve high-performance Li-O2 batteries, Energy Storage Mater. 44 (2022) 285–295. https://doi.org/10.1016/j.ensm.2021.10.026.

[45] P. Márquez, J. Amici, M.J. Aguirre, F. Herrera, C. Francia, S. Bodoardo, Synergic effect of catalyst/binder in passivation side-products of Li-oxygen cells, J. Solid State Electrochem. 23 (2019) 3309–3317. https://doi.org/10.1007/s10008-019-04417-z.

[46] B.D. Adams, C. Radtke, R. Black, M.L. Trudeau, K. Zaghib, L.F. Nazar, Current density dependence of peroxide formation in the Li–O2 battery and its effect on charge, Energy Environ. Sci. 6 (2013) 1772. https://doi.org/10.1039/c3ee40697k.

[47] G. Wang, Y. Li, L. Shi, R. Qian, Z. Wen, Realizing the growth of nano-network Li2O2 film on defect-rich holey Co9S8 nanosheets for Li-O2 battery, Chem. Eng. J. 396 (2020) 125228. https://doi.org/10.1016/j.cej.2020.125228.

[48] R.A. Wong, A. Dutta, C. Yang, K. Yamanaka, T. Ohta, A. Nakao, K. Waki, H.R. Byon, Structurally Tuning Li 2 O 2 by Controlling the Surface Properties of Carbon Electrodes: Implications for Li–O 2 Batteries, Chem. Mater. 28 (2016) 8006–8015. https://doi.org/10.1021/acs.chemmater.6b03751.

[49] W.T. Geng, T. Ohno, Li 2 O 2 Wetting on the (110) Surface of RuO 2 , TiO 2 , and SnO 2 : An Initiating Force for Polycrystalline Growth, J. Phys. Chem. C. 119 (2015)

1024–1031. https://doi.org/10.1021/jp508896s.

[50] G. Sun, Q. Zhao, T. Wu, W. Lu, M. Bao, L. Sun, H. Xie, J. Liu, 3D Foam-Like Composites of Mo 2 C Nanorods Coated by N-Doped Carbon: A Novel Self-Standing and Binder-Free O 2 Electrode for Li–O 2 Batteries, ACS Appl. Mater. Interfaces. 10 (2018) 6327–6335. https://doi.org/10.1021/acsami.7b17795.

[51] H. Yu, K.N. Dinh, Y. Sun, H. Fan, Y. Wang, Y. Jing, S. Li, M. Srinivasan, Q. Yan, Performance-improved Li-O 2 batteries by tailoring the phases of Mo x C porous nanorods as an efficient cathode, Nanoscale. 10 (2018) 14877–14884. https://doi.org/10.1039/C8NR04319A.

[52] L. Wang, Y. Zhang, Z. Liu, L. Guo, Z. Peng, Understanding oxygen electrochemistry in aprotic Li O2 batteries, Green Energy Environ. 2 (2017) 186–203. https://doi.org/10.1016/j.gee.2017.06.004.